Int. J. Electrochem. Sci., 15 **(2020)** 5803 – 5820, doi: 10.20964/2020.06.59

International Journal of
ELECTROCHEMICAL
SCIENCE
www.electrochemsci.org

Loofah Sponge-Derived Sulfur-Rich Porous Carbon with Micropores and Small Mesopores as High Performance Anode Material for Lithium Ion Batteries

Feng Chen[1,‡], *Jiangang Ren*[1,‡], *Lulu Ma*[1], *Xinyu Luo*[2], *Nana Wu*[1], *Shenke Ma*[1], *Bing Li*[1], *Zhiming Song*[1,*], *Xiangyang Zhou*[2,*]

[1] School of Resource and Environment, Henan University of Engineering, No. 1, Xianghe Road, Zhengzhou 451191, China
[2] School of Metallurgy and Environment, Central South University, Lushan South Street 932, Yuelu District, Changsha 410083, China
[*]E-mail: songzhimin1961@hotmail.com (Z.S.); hncsyjy308@163.com (X.Z)
[‡]F.C. and J.R. contributed equally to this work.

Received: 31 January 2020 / *Accepted:* 7 March 2020 / *Published:* 10 May 2020

We reported on the preparation of sulfur-rich porous carbon (SPC) with micropores and small mesopores from natural biomass (loofah sponge) via a high yield, cost-effective, and environmental friendly approach for the first time. The as-obtained SPC was vested with the comprehensive superiority of featuring unique microporous and small mesoporous carbon nanostructure, ultrahigh specific surface area (3211.2 m^2 g^{-1}), inherent doping of sulfur (2.98 wt%), and good electronic conductivity (1.9 S cm^{-1}). The SPC, as the anode material in lithium ion batteries (LIBs), delivered glorious electrochemical characteristics, including a large reversible capacity of 1264.4 mAh g^{-1} at 0.2 C, excellent rate performance (538.6, 351.1, and 256.3 mAh g^{-1} at 2, 5, and 10 C, respectively), and good cycle stability over 400 cycles at 2 C (with 0.087% capacity fading per cycle). The enhanced electrochemical property of SPC was largely ascribed to the cooperative effect of the unique structural features and sulfur doping, which not only could enhance electrochemical activities for lithium storage, but also could promote rapid transfer of lithium ions and electrons. Furthermore, we believe that this work would provide a novel perspective on the reasonable designing of high-energy carbonaceous anode materials.

Keywords: loofah sponge; sulfur-rich carbon; micropores and small mesopores; biomass; lithium ion batteries

1. INTRODUCTION

Rechargeable lithium ion batteries (LIBs) have been significantly applied in hand-held electronics owing to the long cycle lifetime, high-energy density, and environmental benignity [1]. Of

late years, the ever-growing and pressing needs for the widely application in electric vehicles (EVs) and hybrid electric vehicles (HEVs) have vastly sparked the researchers' interests to exploit LIBs with large reversible capacity, superior rate performance and good cycling durability [2-4]. So far, graphite is the most popular anode material for commercial LIBs because of its inexpensive, high electroconductivity, distinguished long-term cycling durability, and relative ease of preparation [5]. Unfortunately, limited theoretical specific capacity (372 mA h g^{-1}) and inferior rate performance are two primary setbacks that restrict further progress of commercialized graphite anode materials [3]. Therefore, persistent attempts have been committed to exploring novel carbonaceous anode materials with improved electrochemical properties for Li^+ storage. Up to now, plenty of novel carbon-based anode materials with varied microstructures have been extensively studied for applications in LIBs, such as graphene [6], porous carbon [7], carbon nanobeads [8], hollow carbon nanospheres [9], and their hybrids [10,11]. However, most of synthetic methods for the above mentioned carbon-based anode materials involve complicated fabrication processes, the consumption of some special reagents, and using high-cost carbon precursors, severely limiting their large-scale applications.

Recently, renewable biomass has attracted significant interest to fabricate carbonaceous anode materials for LIBs owing to its cheap, easily acquiring, huge availability, and harmless to humans. Hence, natural biomass-derived carbonaceous materials as the anodes in LIBs have been exploited with sources as various as bamboo, cotton cellulose, wheat straw, protein, rice husks, banana peels, portobello mushroom, ox horns, and cornstalks [12-20]. Most importantly, those natural biomass-derived porous carbons with nanostructure are particularly attractive because the porous architecture can offer extra active sites for Li^+ storage [4,13]. Furthermore, the large surface area provided by the porous architecture not only can shorten the diffusion distance of Li^+ but also can facilitate sufficient electrode/electrolyte interface that accelerates fast charge-transfer reactions [1,13,14].

The surface chemical modification with heteroatom doping (such as N, B, S, and P) can further enhance the electrochemical properties of carbon-based anode materials [1,6,13,21]. Especially, sulfur (S) element is one of the greatest potential categories of doped heteroatom because the introduction of S atoms into carbon matrix is usually quite helpful to improve its electrical conductivity and chemical activity, which is very conducive to enhance the Li^+ storage capacity. Thus, some S-doped carbons have already been triumphantly utilized as the anode materials in LIBs, such as S-doped amorphous carbon, S-doped mesoporous carbon, S and N dual-doped graphene, S-doped porous carbons hybridized with graphene, and S-doped graphene-based nanosheets [22-26]. Nevertheless, the preparation of these S-doped carbons normally needs the time-consuming fabrication processes, the use of extra sulfur-rich dopants, and expensive carbon sources. Taking the above analysises into consideration, hence, carbon-based anode materials originated from cost-effective reproducible natural resources with adequate porous structure and chemical ingredients might be an ideal choice for LIBs.

Loofah sponge, originated from the totally ripened fruit of climber vine plants (family Cucurbitaceae), is easily obtainable at extremely little cost and prevailing in China and Southeast Asia [27]. Due to its continuous three-dimensional porous network structure, high water/oil uptake, soft tissue, and other characteristics, loofah sponge has already been widely utilized as materials for cleaning cloths during showering and washing, foot pads, automotive filters, and some medical applications, etc [27-29]. Besides, loofah sponge is rich in C elements, O elements, and some other

mineral and nonmetal elements, and hence can easily be pyrolysised into the in situ heteroatomic carbon material with high added-value [30]. Recently, porous carbon derived from loofah sponge exhibits a good prospect of application in microbial fuel cells and supercapacitors [27,31,32]. Thus, considering the particularity of loofah sponge on microstructure and chemical component, its utilization in the preparation of porous carbon anode materials for LIBs would be fully fascinating.

Therefore, in this study, we presented a flexible strategy to synthesize porous carbon that displayed nanoarchitecture with ultrahigh surface area and in situ sulfur doping. The natural loofah sponge was chosen as the raw material and potassium hydroxide served as the activator to generate porous architecture [1,33]. After carbonization of loofah sponge and then activation with KOH, sulfur-rich porous carbon (SPC) with micropores and small mesopores was obtained. The whole synthesis pathway was cost-effective, high yield, and environmental friendly, which was quite suitable for large-scale production. Profiting from the particular structural features and in situ S-doping, the resultant SPC was proven to be an excellent anode material for LIBs in the aspect of large reversible capacity, superior rate capability, and long-term cycling performance. Moreover, so far as we know, it was the first time in the research literatures to report about loofah sponge derived heteroatom-doped porous carbon as the anode material for LIBs.

2. EXPERIMENTAL

2.1. Materials synthesis

The SPC was prepared via pyrolysising the loofah sponge primarily and then activation with KOH. Typically, 20 g of loofah sponge precursor was loaded in a carbon crucible within a tube furnace for the pyrolysis carbonization process at 400 °C for 120 min under nitrogen gas ambience with a heating-up speed of 5 °C min^{-1}, the obtained monolithic carbonized loofah sponge was milled into the powders. Then the as-obtained powders were immersed in the KOH solution (the weight ratio of carbon powder to KOH was 1:4). Afterward, the mixture solutions were dried in an oven at 105 °C and then activated at 800 °C for 1.5 h in a horizontal tube furnace at a flow of N_2 gas with a heating-up speed of 5 °C min^{-1}. At last, the obtained black powder was washed with 1.0 M hydrochloric acid and then deionized water till the filter liquor became neutral. The resulting carbon material was dried overnight at 110 °C in a drying oven, obtaining the final SPC. What's more, the unactivated loofah sponge carbon (named as LSC) was also prepared via carbonization of loofah sponge at 400 °C for 2 h, and afterward at 800 °C for 1.5 h under a flow of N_2 gas except with KOH activation (the other procedures were the same as that of SPC).

2.2. Materials characterization

The morphologies of the acquired specimens were observed with scanning electron microscopy (SEM, Quanta FEG 250, Japan) coupled with an energy dispersive spectrometer (EDS). Transmission electron microscopy (TEM) and high-resolution TEM (HRTEM) were recorded on a JEM-2100F microscope with an EDS. The structure was characterized by X-ray diffraction (XRD, Rigaku-TTRIII, Japan), Fourier transform infrared spectroscopy (FTIR, Thermo Nicolet 6700, Thermo Fisher

Scientific, Waltham, USA), and Raman spectra (LabRAM Hr800, HORIBA Jobin Yvon). The elemental analysis was done by a Vario EL cube Analyzer (Elementar, Frankfurt, Germany). The digital photographs were obtained by a Canon Camera (EOS 750D, Japan). The apparent surface area, pore volume and pore size distributions were calculated by using a Micromeritics ASAP 2020 analyzer. The carbonization process of loofah sponge was traced by Thermogravimetric analysis (TGA, SDTQ600, TA Instruments, New Castle, USA) under nitrogen gas ambience at a heating-up speed of 10 °C min^{-1} from indoor temperature to 900 °C.

2.3. Electrochemical measurements

Electrochemical tests were carried out by using CR2025 button cells with the resultant samples as the working electrode and Li metal foil as the counter electrode. For preparing working electrodes, a mixture of active substance, conductive carbon black, and polyvinylidene fluoride (PVDF) binder at a mass ratio of 8:1:1 dissolved in N-methyl-2-pyrrolidinone (NMP) was uniformly coated on a Cu foil using a doctor blade, and afterward dried at 120 °C overnight under vacuum. The active material loading in the working electrode was approximately 1.0-1.2 mg cm^{-2}. The electrolyte consisted of a solution of 1 M $LiPF_6$ in ethylene carbonate (EC)/dimethyl carbonate (DMC) with a volume ratio of 1:1, and Celgard 2400 was chosen as the separator. The cells were then assembled in an Ar-filled glovebox (Super 1220/750, Shanghai Mikrouna Co. Ltd.). The electrochemical property was investigated on LAND CT-2001A between 0 and 3.0 V vs. Li/Li^+. The initial cycle started at the discharging course, which was corresponded to the insertion of Li^+ into the electrodes. The cyclic voltammogram (CV) was obtained at a scanning rate of 0.2 mV S^{-1} with a cutoff voltage of 0-3.0 V on a PARSTAT 4000 electrochemical workstation. The electrochemical impedance spectroscopy (EIS) was carried out by using the same equipment in the frequency scope 0.01-100 kHz at a charged stage with an automatic scanning mode.

3. RESULTS AND DISCUSSION

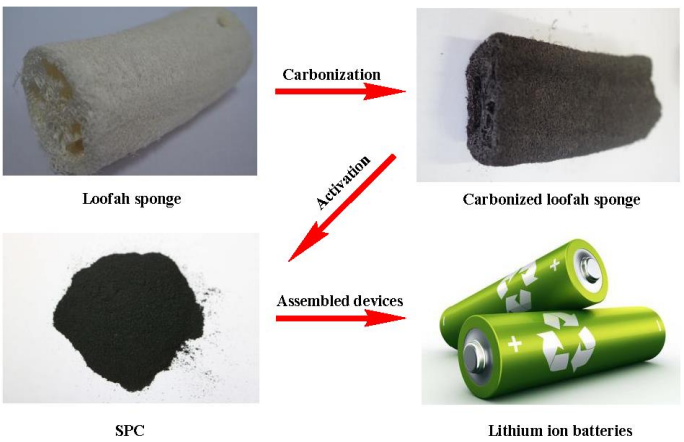

Figure 1. The preparation process of SPC.

A loofah sponge consisted of numerous interleaved continuous ultra-long fibers, exhibiting a

connected macroporous surface and a three-dimensional (3D) network structure (Figure 1). Figure S1a and b displayed the SEM images of loofah sponge, it was clear that the loofah sponge fibres self-crosslinked into a polydirectional array structured with the corrugated surface, and the diameter of these fibers was approximately a few hundred micrometers. The loofah sponge was afterward milled into powders, and the resulting TEM images were displayed in Figure S1c and d. It exposed that loofah sponge powder was a typical lamellar structure, and a number of white dots appeared in the high-resolution TEM image (Figure S1d), demonstrating that affluent micropores existed in the loofah sponge. This goes some way to explaining why loofah sponge was a kind of excellent adsorbent materials. The XRD and Raman spectra of loofah sponge powder were then displayed in Figure S2. The peaks at 2θ=22.4° and 34.4° corresponded to respectively the (002) and (023) crystallographic planes of loofah sponge [34]. In the Raman spectrum of loofah sponge powder, only one strong broad band was observed, which might be ascribed to the fluorescence effect [35]. Therefore, in consideration of its special microscopic morphology and structure, it would be very attractive to convert the loofah sponge into high added-value carbon materials.

The overall preparation process of sulfur-rich porous carbon (SPC) with micropores and small mesopores was illustrated in Figure 1. The loofah sponge precursor was first pyrolyzed directly at nitrogen gas ambience, in order to increase the carbon concentration and produce some pores. Figure S3 showed the TG and DTA curves of loofah sponge powder under a N_2 atmosphere. We can see that the conversion ratio of loofah sponge to carbon was about 14.4 wt%. The obtaining carbon sample was then activated with potassium hydroxide for purpose of generating affluent apertures, and afterward washed with hydrochloric acid and deionized water until pH equaled to 7, acquiring the final SPC sample. The resulting SPC was then applied to the anode material of LIBs. The raw material (loofah sponge) of the preparation process had the merit of inexpensive, rapid reproducibility, enormous availability. What's more, the KOH was extensive used chemical activating agent for carbon materials [33]. Therefore, the whole synthesis pathway for SPC was cost-effective, high yield, and environmental friendly, which was quite suitable for industrial production.

The SEM images of LSC and SPC were first displayed in Figure 2. For LSC, we can see that it showed a typical lamellar structure with the diameter of about a few tens to one hundred microns, and the surface was reversely glossy apart from few small apertures existed on it. However, for SPC, it was obvious that the size of flake nanostructure became smaller, and plenty of holes with various sizes (mesopores and macropores) were discovered on the surface of SPC due to the potassium hydroxide activation effect. Moreover, as shown in Figure S4, the distributions of C, O, and S in SPC were detected by SEM image. The S-rich regions and the O-rich regions overlapped with the C-rich regions absolutely, which testified that we had successfully prepared sulfur-rich carbon materials.

The TEM and HRTEM images of LSC and SPC were then displayed in Figure 3. We can see that both LSC and SPC had a sheet structure with a typical amorphous carbon texture [13]. Moreover, compared to LSC, SPC showed some mesopores and a large number of micropores due to the presence of the speckled contrast synonymous, which might be caused by the KOH activation. The porous structure of SPC could facilitate electrolyte infiltration and provide low-resistant ion passages to promote ion transport [14]. The inset in Figure 3d was the selected-area electron diffraction (SAED) pattern of SPC, further revealing that the carbon substrate was utterly amorphous [36].

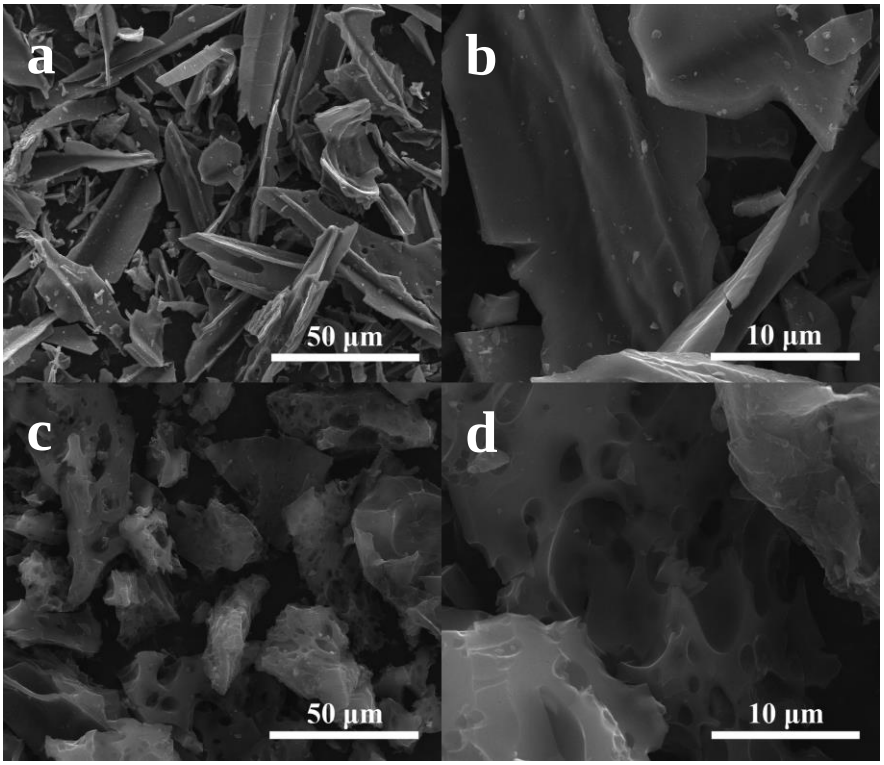

Figure 2. SEM images of LSC (a,b) and SPC (c,d).

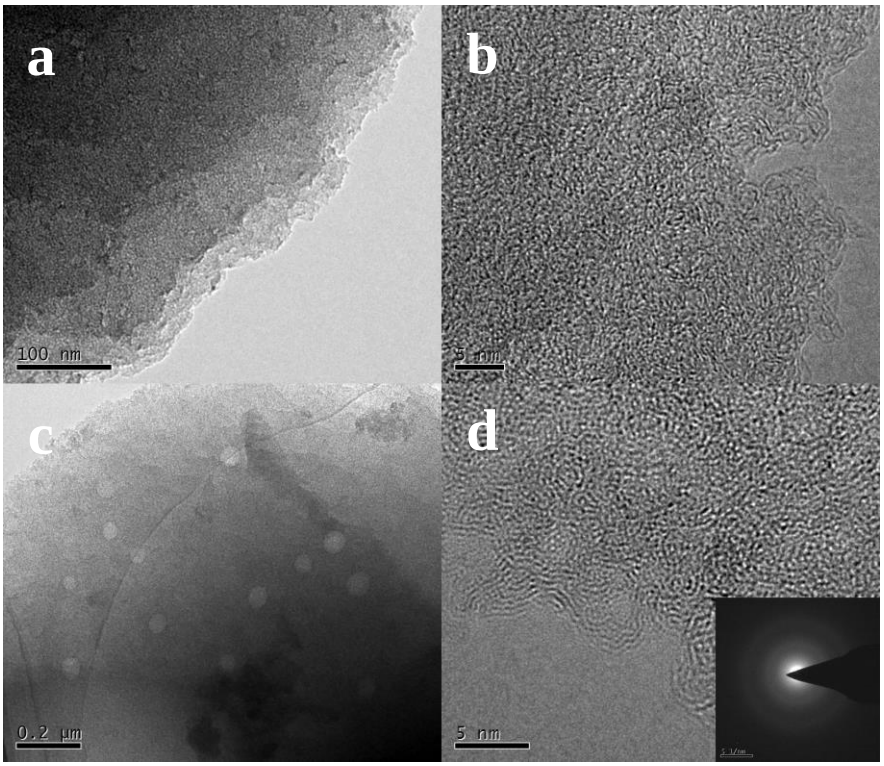

Figure 3. TEM images of LSC (a,b) and SPC (c,d), the inset in (d) is the SAED pattern of SPC.

Figure 4 displayed the TEM image of SPC and the corresponding element maps of C, O, and S by the EDS equipped on the TEM, intensely testifying the successfully incorporated S and O atoms into the SPC forming network, which was consistent well with the above-mentioned elemental maps

analysis by SEM (Figure S4). Moreover, as displayed in Table 1, the element contents of SPC were also measured by a Vario EL cube Analyzer. We can see that the C, H, O, and S contents in SPC were 85.93, 2.04, 6.93, 2.98 wt%, respectively. Therefore, from the above EDS mappings and elemental analyses, it was certain that we had successfully prepared sulfur-rich porous carbon material. The incorporation of S atoms into carbon matrix was usually helpful to enhance its electroconductivity and chemical activity, which would be beneficial to increase the Li^+ storage capacity [22,23].

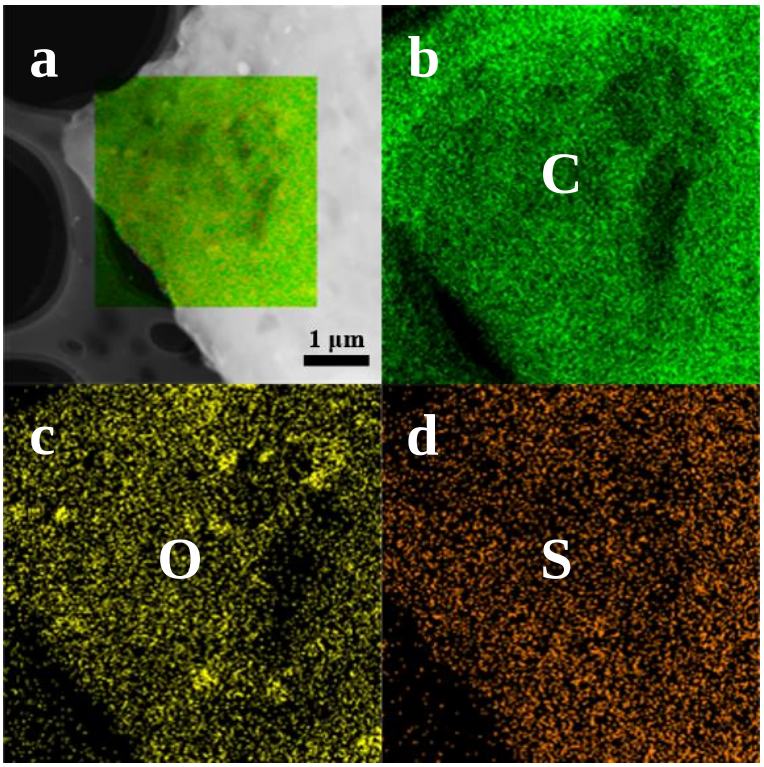

Figure 4. TEM image of SPC (a), corresponding elemental mappings of carbon (b), oxygen (c), and sulfur (d) by the EDS equipped on the TEM.

Table 1. The combustion elemental analysis for SPC.

Sample	C (wt%)	H (wt%)	O (wt%)	S (wt%)
SPC	85.93	2.04	6.93	2.98

The nitrogen adsorption and desorption isotherms were employed to survey the porosity and specific surface area of LSC and SPC, as illustrated in Figure 5a. We can see that both nitrogen adsorption/desorption isotherms of LSC and SPC showed mixed IUPAC type I ($P/P_0<0.1$) and type IV (0.2-0.8 P/P_0) hysteresis, suggesting the presence of typical microporous and mesoporous structure. The pore size distributions for LSC and SPC were then calculated according to the desorption branch based on a density functional theory (DFT) model and were displayed in the Figure 5b. Apparently, the LSC sample primarily consisted of micropores less than 2 nm, whereas the SPC sample was primarily comprised of micropores within the scope of 0.6-2.0 nm and diminutive mesopores which had a

maximum around 2.1 nm. The pore diameter of under 0.6 nm couldn't be detected on account of the limitation of the analyzer. The porosity results of LSC and SPC matched with the SEM and TEM analyzes well (Figure 2 and 3). Table 2 summarized the specific surface area, total pore volume, micropore volume, and mean pore size of LSC and SPC. The BET specific surface area and total pore volume of LSC were respectively 628.7 m^2 g^{-1} and 0.33 cm^3 g^{-1}. However, for SPC, the specific surface area was larger (3211.2 m^2 g^{-1}), and the total pore volume was higher (1.72 cm^3 g^{-1}), which might arise from the activation effect of KOH. The micropore volume of SPC (1.61 cm^3 g^{-1}) was much larger than that of LSC (0.27 cm^3 g^{-1}) calculated by t-plot method. Moreover, the micropore volume for SPC accounted for 93.6% of the total pore volume, which further demonstrated its microporous and small mesoporous structure. Such a hierarchical porous architecture of SPC not merely could afford additional active sites for Li^+ storage, but also could promote adequate electrode/electrolyte interface to adsorb Li^+ and facilitate fast charge-transfer reactions, thus remarkably enhance the electrochemical property of the LIBs [1,13,14].

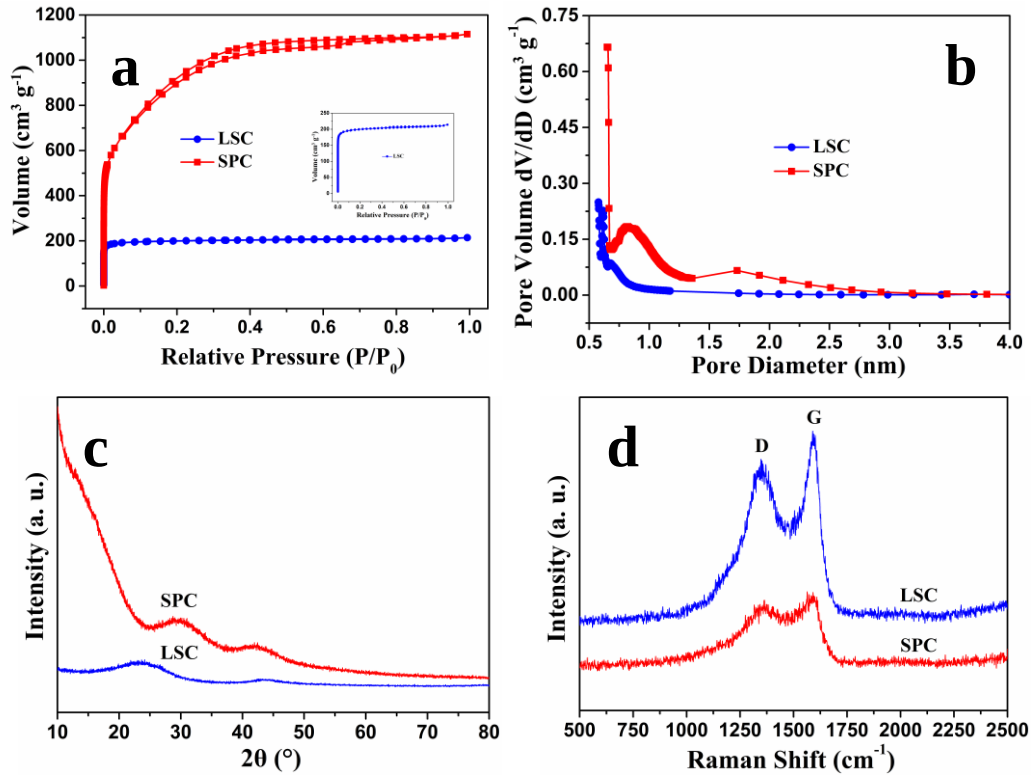

Figure 5. Nitrogen adsorption and desorption isotherms (a), pore size distribution curves (b), XRD spectra (c), and Raman spectra (d) of LSC and SPC.

Table 2. The primary pore parameters of LSC and SPC.

Sample	Specific surface area (m^2 g^{-1})	Total pore volume (cm^3 g^{-1})	Micropore volume (cm^3 g^{-1})	Average pore size (nm)
LSC	628.7	0.33	0.27	2.11
SPC	3211.2	1.72	1.61	2.15

X-ray diffraction (XRD) spectra of LSC and SPC were displayed in Figure 5c. Two broad characteristic diffraction peaks were situated at 20°~30° and 40°~50°, which were associated with the (002) and (100) facets of graphite (JCPDS no. 41-1487), respectively. Moreover, no obvious sharp peaks were surveyed in the XRD spectra of both samples, indicating their amorphous carbon structure. It had been reported that the amorphous carbon was conducive to Li^+ insertion and deinsertion [37]. Raman spectroscopy can also be used to gain structural information of the carbon materials. As exhibited in Figure 5d, the Raman spectra of LSC and SPC displayed two well-known fingerprint peaks, involving D band (~1350 cm^{-1}) and G band (~1590 cm^{-1}). The D band was related to some defects, edges, and disordered carbon, while the G band was identified as the crystalline graphite structure [14,33]. This indicated the partial graphitization of SPC due to the activation course with KOH at 800 °C, which was beneficial to promote its conductivity. Moreover, the intensity ratio of I_D/I_G could survey the degree of disorder and the mean dimension of the sp^2 domains [38]. The higher strength ratio of I_D/I_G in SPC (0.95) indicated a higher degree of disorder, more defects, or abundant element doping compared to that in LSC (I_D/I_G=0.91), which favored an improved reversible capacity of the anode materials and an enhancement the Li^+ storage capacity [14,39].

Further structure information of SPC was acquired by FTIR analysis (Figure 6). The adsorption bands at 684, 811, 1091, and 2358 cm^{-1} were attributed to the stretching vibrations of C-S, S-S, S-O, and S-H bonds, respectively [40,41]. The peak at 1219 cm^{-1} was ascribed to the C-S, and C-O stretching vibrations [41]. In addition, the peak between 1403 and 1486 cm^{-1} could be considered as the COO^- groups. The 1588 and 1689 cm^{-1} bands were allotted to the breathing vibrations of C=C and C=O, and the broad band centered at 3422 cm^{-1} appeared on account of the O-H bonds [41,42]. Therefore, the FTIR spectrum obviously demonstrated the presence of S/O-containing functional groups on the surface of SPC, which compared well with the results of EDS and elemental analysis (Figure 4 and Table 1). The sulfur doping in the SPC was beneficial to the improvement of electric conductivity and the formation of more defects, both of which could enhance the electrochemical properties of the carbon materials [22-26].

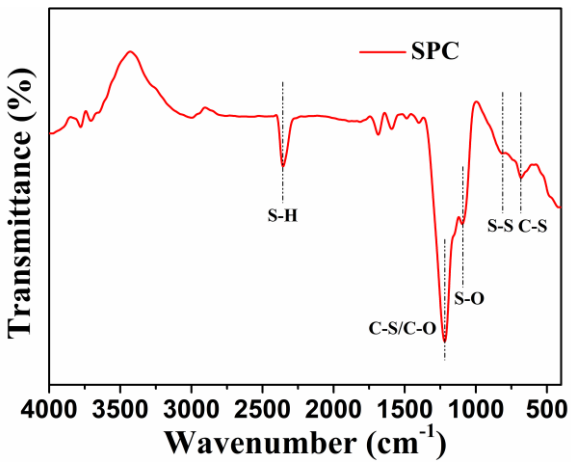

Figure 6. FTIR spectrum of SPC.

The electrochemical properties of both LSC and SPC were then assessed by using 2025 coin-type cells via galvanostatic charge/discharge cycling in the potential range 0-3.0 V vs. Li/Li^+ at various current densities. The CV profiles of SPC recorded in the initial five cycles were first shown in Figure 7a, which was classic for amorphous carbon anode materials [15,21]. In the first reduction scan, one prominent irreversible peak occurred between 0.4-0.7 V was surveyed, which radically vanished in the following cycles. This was concerned with the inconvertible decomposition of electrolyte via the formation of solid electrolyte interphase (SEI) film, as well as with the nonreversible loss of some Li^+ insertion sites in the carbon structure [3,15]. After the 1st cycle, the CV curves exhibited a good repeatability, indicating the superior cycle reversibility of the SPC electrode.

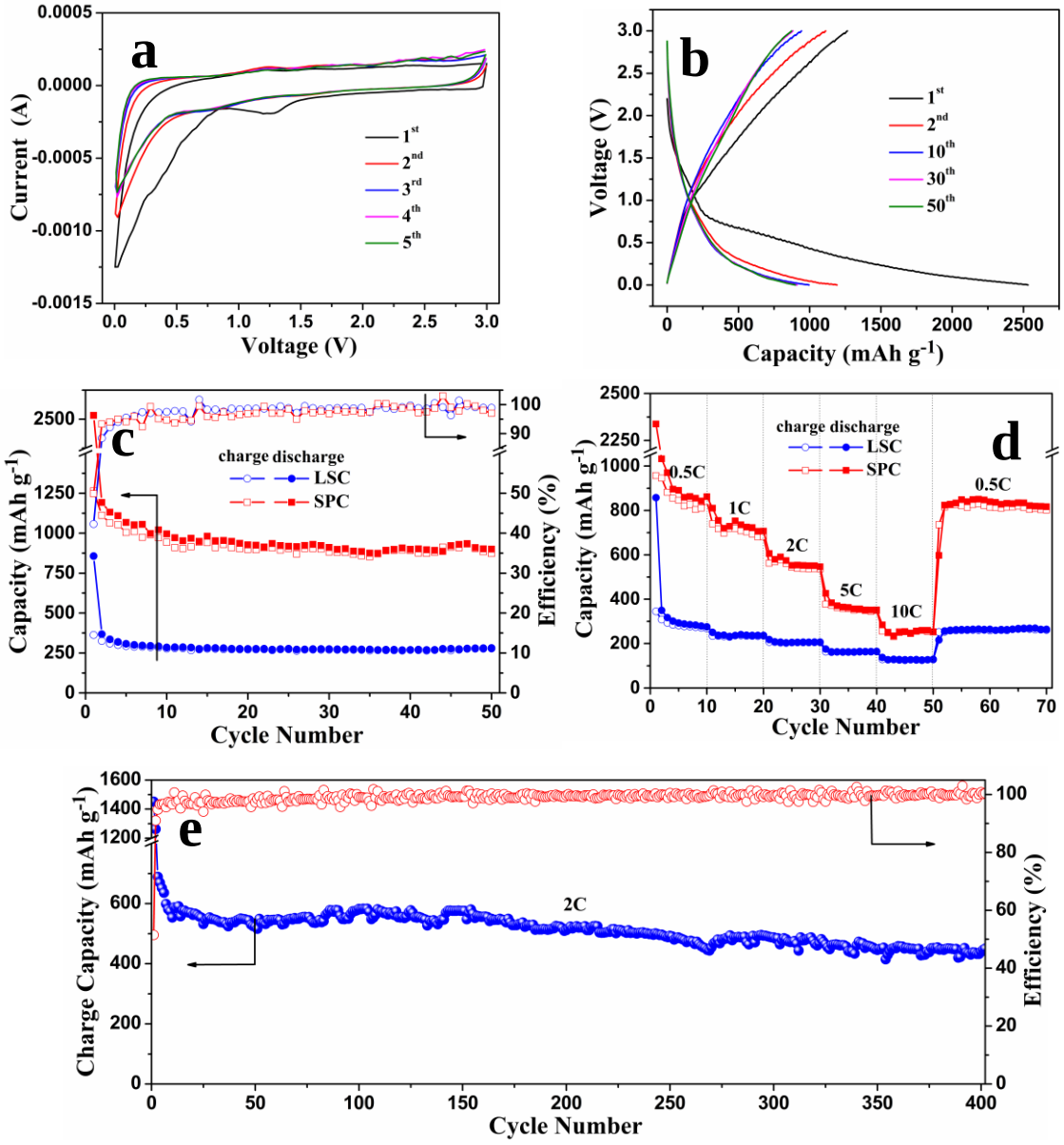

Figure 7. (a) Cyclic voltammogram (CV) curves of SPC at a scanning rate of 0.2 mV S^{-1} for the initial five cycles, (b) galvanostatic charge/discharge profiles of SPC in the potential range 0-3.0 V vs. Li/Li^+ at 0.2 C, (c) cycling performances of LSC and SPC for 50 cycles under 0.2 C, (d) rate performances of LSC and SPC under various current densities from 0.5 to 10 C, (e) long cycling capability of SPC at current density of 2 C.

Figure S5 and 7b displayed the charge/discharge curves of LSC and SPC at 0.2 C. The SPC electrode exhibited a specific capacity of up to 1264.4 mAh g^{-1} during the initial cycle, which was approximately 3.4 times higher than that of natural graphite (372 mAh g^{-1}), and was also higher than that of the LSC electrode (362.5 mAh g^{-1}). Meanwhile, a large irreversible capacity of 1267.7 mAh g^{-1} also displayed in the SPC electrode, which was a very universal outcome in the carbonaceous electrodes [6,9]. The coulombic efficiency increased from 42.3% for the LSC electrode to 49.9% for the SPC electrode in the initial cycle, which proved that the sulfur-doping could, in some ways, repress the electrolyte decomposition and secondary reactions between the SPC electrode and electrolyte to form the SEI layer. Further, the shape of the charge/discharge profiles for both LSC and SPC electrodes was very alike to those carbon anode materials as previously reported. As shown in Figure 7c, the SPC electrode still remained a reversible specific capacity of 873.1 mAh g^{-1} after 50 cycles at 0.2 C, which was much larger than that of the LSC electrode (278.2 mAh g^{-1}), revealing a good cycling property and reversibility.

In order to acquire more evidence of the enhanced electrochemical property of SPC, raised current densities were further carried out to research the rate capabilities of both LSC and SPC electrodes in the identical conditions, as illustrated in Figure 7d. The SPC electrode delivered the reversible capacities of 820.3, 703.4, 538.6, and 351.1 mAh g^{-1} at 0.5, 1, 2, and 5 C, respectively. A highly specific capacity of 256.3 mAh g^{-1} was still exhibited even at 10 C. It's also worth noting that the SPC owned an excellent reversibility as the capacity was recovered to 816.7 mAh g^{-1} after 70 cycles when the ampere density switched back to 0.5 C abruptly. Moreover, all the reversible capacities of SPC electrode seemed to be much higher than those of LSC electrode at the same current densities. The charge/discharge graphs of LSC and SPC electrodes under various current densities from 0.5 to 10 C displayed the typical "V" type curves and also confirmed this conclusion (Figure S6). The striking contrast in cycling property and rate capability between the LSC and SPC electrodes highly suggested that the large specific area, unique microporous structure, and in situ S-doping could provide synergistic effects on improving electrochemical properties tremendously. What's more, the comparison of the performances of lithium ion batteries used SPC and those of some other carbon materials derived from biomass as anodes were then showed in Table 3. We can see that the initial reversible capacity and rate capability of SPC were better than those of some other biomass-based carbon anode materials ever reported [13,16,43-47].

To further affirm its superior Li^+ storage performances for long-range cycling, the SPC electrode was then evaluated at a high ampere density of 2 C (Figure 7e). The SPC electrode was first cycled at 0.2 C to activate the cell for two cycles. We can see that a reversible charge capacity of 688.9 mAh g^{-1} was delivered in the first cycle at 2 C. Upon completion of even 400 cycles, the reversible capacity of SPC electrode could still maintain 450.2 mAh g^{-1}, along with a low capacity decay rate of 0.087% per cycle. In addition, the average coulombic efficiency was about 99.0%, reflecting a good reversibility of Li^+ storage. The possibilities of the significantly improved electrochemical performances of the SPC electrode could be explained by the following virtues of the SPC (Figure 8). First, the unique nanosheet architecture and good electrical conductivity could tremendously shorten the diffusion lengths for Li^+, and also could provide a rapid and consecutive pathway for electrons transfer [1,3,9]. To confirm this standpoint, we surveyed the conductivity of SPC employing a classic

four-point probe method, and the measured value reached up to 1.9 S cm^{-1}. Second, the large surface area provided by the microporous and small mesoporous structure not merely could offer more lithium storage active sites, but also could promote adequate electrode/electrolyte interface to adsorb Li^+ and facilitate fast charge transfer reactions [4,13,14,20]. Third, the sulfur doping in the SPC could further improve the electronic conductivity and electrochemical activity, which additionally contributed to the outstanding performances [22-26].

Table 3. Comparison of the performances of lithium ion batteries used SPC and those of some other carbon materials derived from biomass as anodes.

Sample	Carbon source	Initial reversible capacity (mAh g^{-1})	Rate capability (mAh g^{-1})	Reference
Heteroatom-enriched amorphous carbon	Cotton cellulose	935 (0.13C)	240 (5.4C)	[13]
Rice husk-derived carbon	Rice husk	789 (0.2C)	137 (10C)	[16]
Porous carbon	Rice hull	~730 (0.2C)	154.6 (5C)	[43]
Structurally tunable carbon	Wheat flour	405 (0.1C)	~180 (1C)	[44]
Mesoporous activated carbon	Corn stalk core	760.3 (0.2C)	275 (5C)	[45]
Hierarchical porous carbon	Lignin	513.9 (0.54C)	268 (2.7C)	[46]
Biomass-derived pyrolytic carbon	Green tea	530 (0.1C)	131 (10C)	[47]
Sulfur-rich porous carbon	Loofah sponge	1264.4 (0.2C)	351.1 (5C)/ 256.3 (10C)	This work

Figure 8. Schematic diagram of electron transport and Li^+ storage in the SPC electrode.

For the sake of shedding new light on the transport kinetics for the outstanding electrochemical performances of SPC, the electrochemical impedance spectroscopy (EIS) tests for the LSC and SPC electrodes before cycling and after 50 cycles at 0.2 C were carried out. As exhibited in Figure 9a, note that the Nyquist plots of both electrodes before cycling were composed of a depressed semicircle in the high-to-medium frequency area and an oblique line in the low-frequency region. In the relevant equivalent circuit model, R_e represented the total resistance of the cell, which included the electrode, electrolyte, and separator impedances. R_{ct} represented the charge-transfer resistance on the electrolyte/

electrode interface. Z_w was the Warburg impedance related to the solid-state lithium diffusion process within the bulk electrodes [19,24,48]. However, two depressed semicircles were obviously observed from the Nyquist plots of both electrodes after 50 cycles at 0.2 C (Figure 9b). The newly emerged R_f in the equivalent circuit model was the resistance for lithium ion migration through the SEI film [49,50].

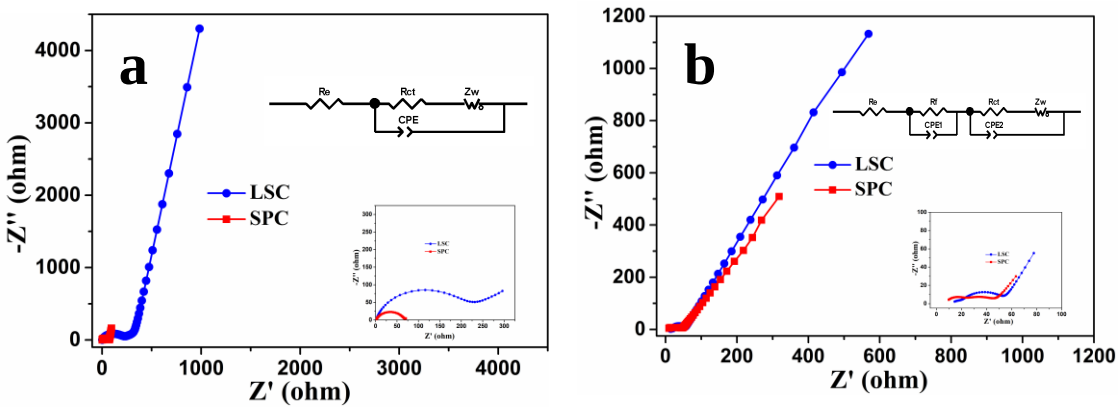

Figure 9. Typical Nyquist plots recorded for the LSC and SPC electrodes before cycling (a) and after 50 cycles at 0.2 C (b), the insets are the relevant equivalent circuit models.

The EIS was modeled via the typical equivalent circuits (the insets in Figure 9a and b) and the resulting kinetic parameters of the LSC and SPC electrodes were summarized in Table 4. The R_e and R_{ct} values for the SPC electrode (1.23 and 65.76 Ω) were smaller than those of the LSC electrode (1.29 and 206.40 Ω) before cycling, indicating a high electronic conductivity and low charge-transfer resistance of the SPC electrode [49]. After 50 cycles, the R_{ct} values for both electrodes were dramatically reduced compared to those observed before cycling, which was a very common phenomenon as previously reported [19,49]. What's more, the values of R_f and R_{ct} for the SPC electrode were 11.04 and 30.85 Ω respectively, which were much lower than those of the LSC electrode (12.01 and 32.29 Ω), manifesting that the SPC electrode had a thinner SEI layer, favoring fast lithium ion insertion and extraction as well as facile charge-transfer reaction at the electrolyte/ electrode interphase [24].

Table 4. Kinetic parameters of the LSC and SPC electrodes imitated from the equivalent circuit fitting of experiment data.

Sample	Cycle number	R_e (Ω)	R_f (Ω)	R_{ct} (Ω)
LSC	Before cycling	1.29	—	206.40
	After 50 cycles	11.12	12.01	32.29
SPC	Before cycling	1.23	—	65.76
	After 50 cycles	7.22	11.04	30.85

4. CONCLUSIONS

In this work, sulfur-rich porous carbon (SPC) with micropores and small mesopores has been successfully synthesized via the directly pyrolyzed of natural loofah sponge followed by further KOH activation for the first time. The resultant SPC was vested with the comprehensive superiority of featuring unique microporous and small mesoporous carbon nanostructure, ultrahigh specific surface area, intrinsic doping of sulfur, and good electronic conductivity. As the anode material in lithium ion batteries, the SPC showed large reversible capacity (1264.4 mAh g^{-1} at 0.2 C), superior rate capability (256.3 mAh g^{-1} at 10 C), and good stable cyclability (maintained a reversible capacity of 450.2 mAh g^{-1} over 400 cycles at 2 C with a low capacity fading rate of 0.087% per cycle). Our work indicated that the SPC was a promising anode material for the next generation rechargeable lithium ion batteries. What's more, we firmly believed that the acquired SPC might also be applied to the other fields like pollutant absorption, supercapacitor, biosensors, and hydrogen storage, etc.

CONFLICT OF INTERESTS

The authors declare that there is no conflict of interests regarding the publication of this paper.

ACKNOWLEDGMENTS

Funding for this work was provided by the National Natural Science Foundation of China (51204209, 51274240, and 41872169), the Key Scientific and Technological Project of Henan Province (192102310464), the Henan Young Talents Supporting Project in 2019 (2019HYTP012), the Key Scientific Research Projects of Henan Colleges and Universities (19A610004), the Innovation Training Program for College Students of Henan Province (S201911517007), the Doctoral Scientific Fund Project of Henan University of Engineering (D2017011), and the Project of 543 Innovation-driven Plan in Henan University of Engineering.

SUPPLEMENTARY MATERIAL

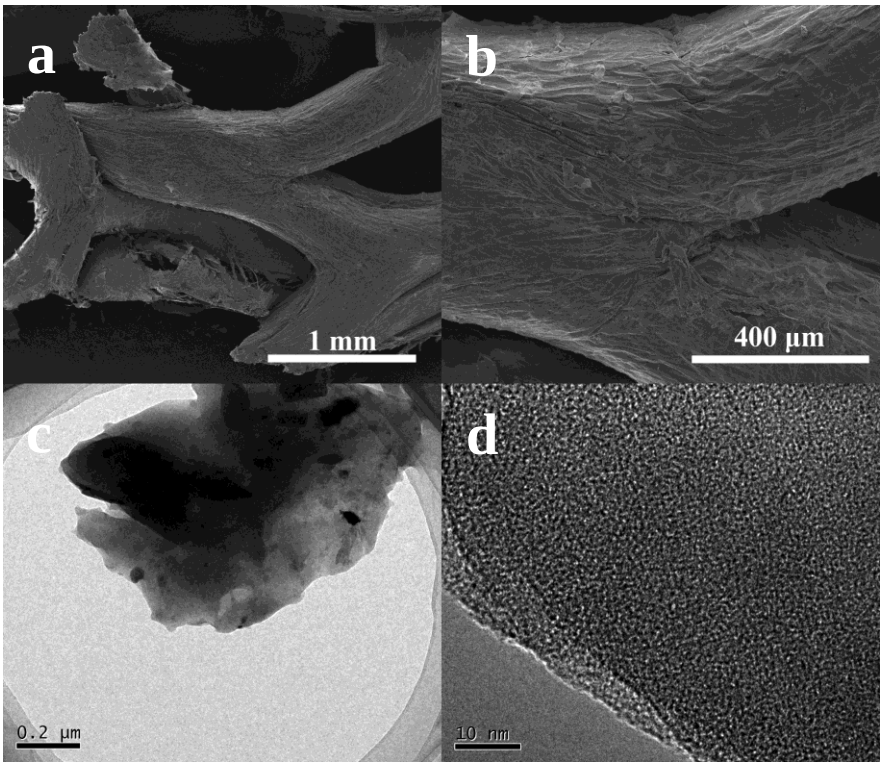

Figure S1. SEM images of loofah sponge (a-b), TEM images of loofah sponge powder (c-d).

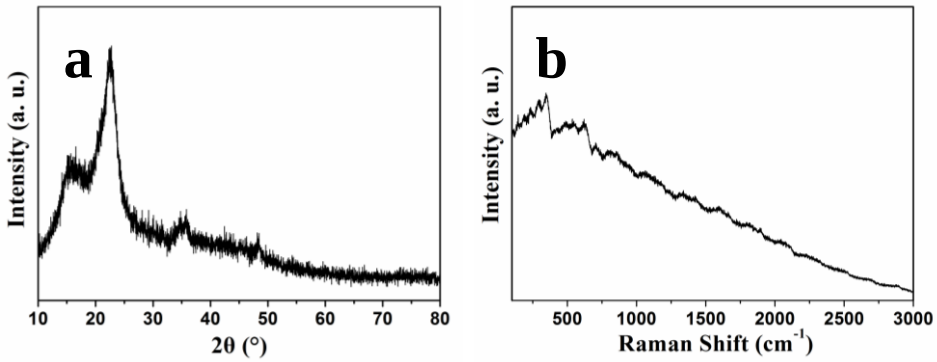

Figure S2. (a) XRD spectrum of loofah sponge powder, (b) Raman spectrum of loofah sponge powder.

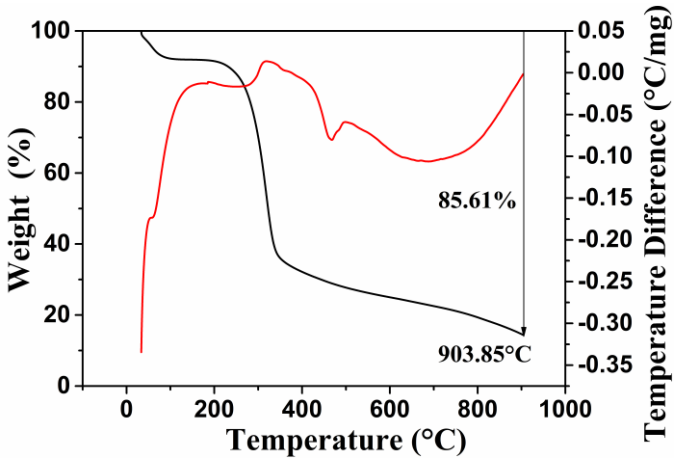

Figure S3. TGA curve of loofah sponge powder.

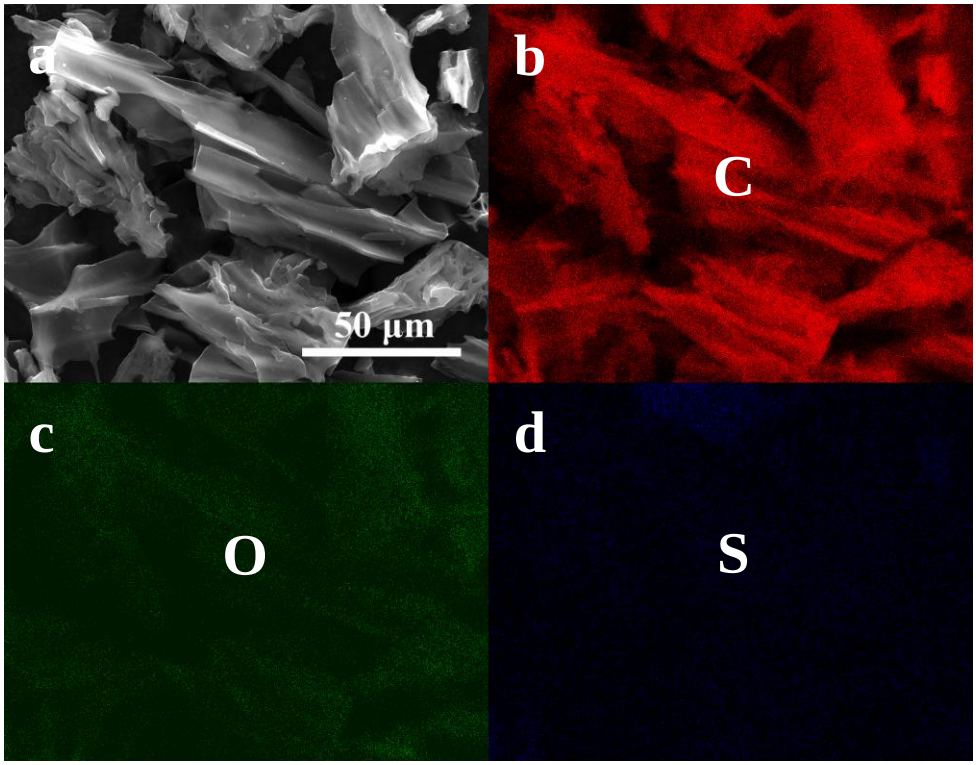

Figure S4. SEM image of SPC (a), corresponding elemental maps of C (b), O (c), and S (d).

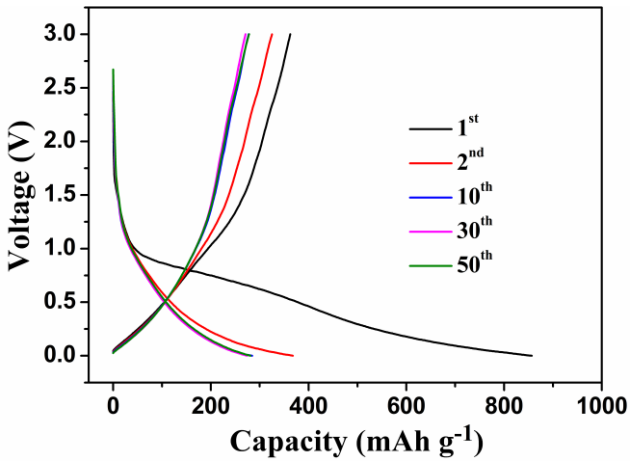

Figure S5. Galvanostatic charge/discharge profiles of LSC in the potential range 0-3.0 V vs. Li/Li^+ at 0.2 C.

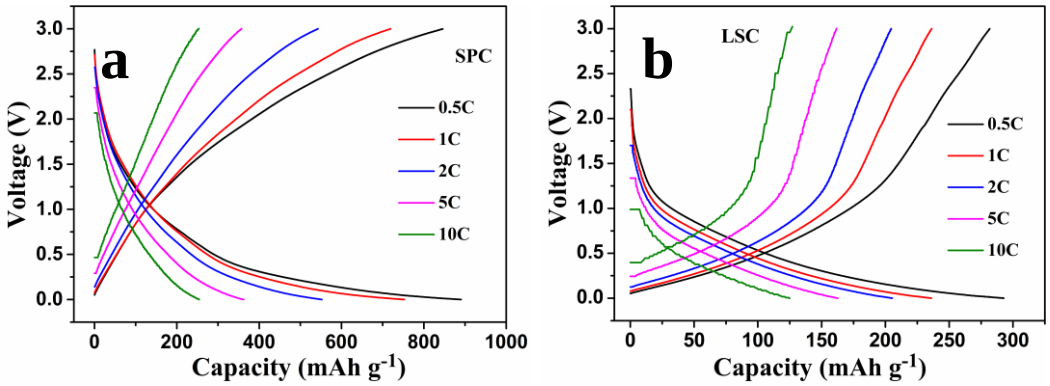

Figure S6. Galvanostatic charge/discharge profiles of SPC (a) and LSC (b) under various current densities from 0.5 to 10 C.

References

1. L. Qie, W. M. Chen, Z. H. Wang, Q. G. Shao, X. Li, L. X. Yuan, X. L. Hu, W. X. Zhang and Y. H. Huang, *Adv. Mater.*, 24 (2012) 2047.
2. J. Yan, X. Liu and B. Li, *RSC Adv.*, 4 (2014) 63268.
3. X. Zhou, F. Chen, T. Bai, B. Long, Q. Liao, Y. Ren and J. Yang, *Green Chem.*, 18 (2016) 2078.
4. Y. Chen, Z. Lu, L. Zhou, Y. W. Mai and H. Huang, *Nanoscale*, 4 (2012) 6800.
5. W. Fang, X. Cheng, P. Zuo, Y. Ma and G. Yin, *Electrochim. Acta*, 93 (2013) 173.
6. Z. S. Wu, W. Ren, L. Xu, F. Li and H. M. Cheng, *ACS Nano*, 5 (2011) 5463.
7. K. T. Lee, J. C. Lytle, N. S. Ergang, S. M. Oh and A. Stein, *Adv. Funct. Mater.*, 15 (2010) 547.
8. H. Wang, T. Abe, S. Maruyama, Y. Iriyama, Z. Ogumi and K. Yoshikawa, *Adv. Mater.*, 17 (2005) 2857.
9. F. D. Han, Y. J. Bai, R. Liu, B. Yao, Y. X. Qi, N. Lun and J. X. Zhang, *Adv. Energy Mater.*, 1 (2011) 798.
10. S. Li, Y. Luo, W. Lv, W. Yu, S. Wu, P. Hou, Q. Yang, Q. Meng, C. Liu and H. M. Cheng, *Adv. Energy Mater.*, 1 (2011) 486.
11. J. Zhang, Y. S. Hu, J. P. Tessonnier, G. Weinberg, J. Maier, R. Schlögl and D. S. Su, *Adv. Mater.*, 20 (2008) 1450.
12. J. Jiang, J. Zhu, W. Ai, Z. Fan, X. Shen, C. Zou, J. Liu, H. Zhang and T. Yu, *Energy Environ. Sci.*, 7 (2014) 2670.

13. Y. S. Yun and H. J. Jin, *Mater. Lett.*, 108 (2013) 311.
14. L. Chen, Y. Zhang, C. Lin, W. Yang, Y. Meng, Y. Guo, M. Li and D. Xiao, *J. Mater. Chem. A*, 2 (2014) 9684.
15. Z. Li, Z. Xu, X. Tan, H. Wang, C. M. B. Holt, T. Stephenson, B. C. Olsen and D. Mitlin, *Energy Environ. Sci.*, 6 (2013) 871.
16. L. Wang, Z. Schnepp and M. M. Titirici, *J. Mater. Chem. A*, 1 (2013) 5269.
17. E. M. Lotfabad, J. Ding, K. Cui, A. Kohandehghan, W. P. Kalisvaart, M. Hazelton and D. Mitlin, *ACS Nano*, 8 (2014) 7115.
18. B. Campbell, R. Ionescu, Z. Favors, C. S. Ozkan and M. Ozkan, *Sci. Rep.*, 5 (2015) 14575.
19. J. Ou, Y. Zhang, L. Chen, Q. Zhao, Y. Meng, Y. Guo and D. Xiao, *J. Mater. Chem. A*, 3 (2015) 6534.
20. S. Wang, C. Xiao, Y. Xing, H. Xu and S. Zhang, *J. Mater. Chem. A*, 3 (2015) 6742.
21. J. Wang, Z. Yang, F. Pan, X. Zhong, X. Liu, L. Gu and Y. Yu, *RSC Adv.*, 5 (2015) 55136.
22. Y. P. Wu, S. Fang, Y. Jiang and R. Holze, *J. Power Sources*, 108 (2002) 245.
23. S. Zhang, F. Yao, L. Yang, F. Zhang and S. Xu, *Carbon*, 93 (2015) 143.
24. X. Ma, G. Ning, Y. Sun, Y. Pu and J. Gao, *Carbon*, 79 (2014) 310.
25. Y. Yan, Y. X. Yin, S. Xin, Y. G. Guo and L. J. Wan, *Chem. Commun.*, 48 (2012) 10663.
26. Y. S. Yun, V. D. Le, H. Kim, S. J. Chang, S. J. Baek, S. Park, B. H. Kim, Y. H. Kim, K. Kang and H. J. Jin, *J. Power Sources*, 262 (2014) 79.
27. Y. Yuan, S. Zhou, Y. Liu and J. Tang, *Environ. Sci. Technol.*, 47 (2013) 14525.
28. A. Altinisik, E. Gur and Y. Seki, *J. Hazard. Mater.*, 179 (2010) 658.
29. K. E. Bal, Y. Bal, G. Cote and A. Chagnes, *Mater. Lett.*, 79 (2012) 238.
30. R. Ravella, M. Reddy, K. Taylor and M. Miller, *Am. J. Exp. Agric.*, 5 (2015) 475.
31. J. Li, Z. Ren, Y. Ren, L. Zhao, S. Wang and J. Yu, *RSC Adv.*, 4 (2014) 35789.
32. Y. Luan, Y. Huang, L. Wang, M. Li, R. Wang and B. Jiang, *J. Electroanal. Chem.*, 763 (2016) 90.
33. F. Chen, J. Yang, T. Bai, B. Long and X. Zhou, *Electrochim. Acta*, 192 (2016) 99.
34. L. Ghali, S. Msahli, M. Zidi and F. Sakli, *Mater. Lett.*, 63 (2009) 61.
35. L. Chai, J. Wang, H. Wang, L. Zhang, W. Yu and L. Mai, *Nano Energy*, 17 (2015) 224.
36. J. Yang, F. Chen, C. Li, T. Bai, B. Long and X. Zhou, *J. Mater. Chem. A*, 4 (2016) 14324.
37. D. Pan, S. Wang, B. Zhao, M. Wu, H. Zhang, Y. Wang and Z. Jiao, *Chem. Mater.*, 21 (2009) 3136.
38. K. Wu, K. Du and G. Hu, *J. Mater. Chem. A*, 6 (2018) 3444.
39. G. Li, W. Lei, D. Luo, Y. P. Deng, D. Wang and Z. Chen, *Adv. Energy Mater.*, 8 (2018) 1702381.
40. D. Sun, R. Ban, P. H. Zhang, G. H. Wu, J. R. Zhang and J. J. Zhu, *Carbon*, 64 (2013) 424.
41. W. Li, M. Zhou, H. Li, K. Wang, S. Cheng and K. Jiang, *Energy Environ. Sci.*, 8 (2015) 2916.
42. Y. Hu, J. Yang, J. Tian, L. Jia and J. S. Yu, *Carbon*, 77 (2014) 775.
43. K. Yu, Y. Wang, X. Wang, W. Liu, J. Liang and C. Liang, *Mater. Lett.*, 253 (2019) 405.
44. D. G. Lim, K. Kim, M. Razdan, R. Diaz, S. Osswald and V. G. Pol, *Carbon*, 121 (2017) 134.
45. Y. Li, C. Li, H. Qi, K. Yu and C. Liang, *Chem. Phys.*, 506 (2018) 10.
46. W. Zhang, J. Yin, Z. Lin, H. Lin, H. Lu, Y. Wang and W. Huang, *Electrochim. Acta*, 176 (2015) 1136.
47. S. W. Han, D. W. Jung, J. H. Jeong and E. S. Oh, *Chem. Eng. J.*, 254 (2014) 597.
48. R. Song, H. Song, J. Zhou, X. Chen, B. Wu and H. Y. Yang, *J. Mater. Chem.*, 22 (2012) 12369.
49. M. Li, H. Song, X. Chen, J. Zhou and Z. Ma, *Phys. Chem. Chem. Phys.*, 17 (2015) 3250.
50. S. Yang, X. Feng, L. Zhi, Q. Cao, J. Maier and K. Mullen, *Adv. Mater.*, 22 (2010) 838.